Iranian Journal of Numerical Analysis and Optimization
Vol. ??, No. ??, ??, pp ??
https://doi.org/??
https://ijnao.um.ac.ir/

Research Article

Unraveling the relationship between COVID-19 viral load, disease severity, and innate immune response: Insights from mathematical modeling and sensitivity analysis

M. Lotfi, A. Jabbari*, R. Rahbarghazi and H. Kheiri

Abstract

Coronavirus disease 2019 (COVID-19) created a global health crisis and highlighted the need for a mechanistic understanding of the interactions between SARS-CoV-2 and host immune responses. Although numerous mathematical models have described COVID-19 at the epidemiological scale, fewer studies have examined within-host viral dynamics and innate immune

*Corresponding author

Received ??? ; revised ??? ; accepted ???

Mehdi Lotfi
Institute of Bioinformatics, University Medicine Greifswald, Greifswald, Germany.

Azizeh Jabbari
Department of Applied Mathematics, Faculty of Mathematical Sciences, University of Tabriz, Tabriz, Iran. e-mail: a_jabari@tabrizu.ac.ir

Reza Rahbarghazi
Department of Applied Cell Sciences, Faculty of Advanced Medical Sciences, Tabriz University of Medical Sciences, Tabriz, Iran.

Hossein Kheiri
Department of Applied Mathematics, Faculty of Mathematical Sciences, University of Tabriz, Tabriz, Iran.

How to cite this article
Lotfi, M., Jabbari, A., Rahbarghazi, R. and Kheiri, H., Unraveling the relationship between COVID-19 viral load, disease severity, and innate immune response: Insights from mathematical modeling and sensitivity analysis. *Iran. J. Numer. Anal. Optim.*, ??; ??(??): ??-??. ??

mechanisms. In this study, we develop a nonlinear ordinary differential equation model describing interactions among SARS-CoV-2, epithelial cells, resting and activated macrophages, neutrophils, and monocytes. We establish the nonnegativity of solutions, derive the within-host basic reproduction number, and analyze the local and global stability of the COVID-19-free equilibrium. Parameters are calibrated using two clinical datasets representing mild, severe, and intensive care unit (ICU) cases. The calibrated simulations indicate that mild disease is associated with faster viral clearance, more effective immune-mediated viral removal, and better epithelial recovery, whereas severe and ICU cases exhibit delayed clearance, dysregulated neutrophil dynamics, and greater virus-associated immune-cell loss. The corrected normalized sensitivity indices show that viral entry, healthy epithelial-cell renewal, infected-cell lysis, and viral production increase the basic reproduction number, whereas infected-cell recovery, cell loss, and viral clearance reduce it. These findings provide quantitative insight into how innate immune dysregulation may contribute to COVID-19 severity and identify the model mechanisms that most strongly influence within-host viral persistence.

AMS subject classifications (2020): Primary 34A34; Secondary 34D20, 92C37.

Keywords: SARS-CoV-2; COVID-19; innate immune dynamics; within-host modeling; sensitivity analysis.

1 Introduction

Infectious-disease outbreaks have historically posed major threats to human societies. The Plague of Justinian in the sixth century and the Black Death in the fourteenth century caused substantial mortality, while smallpox and cholera have also profoundly affected global health [13, 17]. These examples illustrate the persistent influence of infectious diseases on human survival and social development.

In late 2019, a novel coronavirus, subsequently named severe acute respiratory syndrome coronavirus 2 (SARS-CoV-2), was identified in Wuhan, Hubei Province, China, in association with severe respiratory illness. Despite early containment efforts, the virus spread rapidly and resulted in a global pandemic. By 13 July 2021, more than 186 million confirmed infections and 4 million deaths had been reported worldwide [26]. SARS-CoV-2 primarily affects the respiratory tract and can produce symptoms including fever, cough, fatigue, dyspnea, and myalgia [4].

Coronaviruses are enveloped, single-stranded RNA viruses belonging to the family *Coronaviridae*. They infect several animal species and humans. SARS-CoV-2 is transmitted predominantly through respiratory particles, particularly during close contact. Since the beginning of

the pandemic, extensive research has focused on vaccines, antiviral treatments, and supportive clinical management.

Many epidemiological models have evaluated the effects of self-isolation, mask use, social distancing, hygiene practices, and other public-health interventions on COVID-19 transmission [8, 14, 19, 20, 21]. In contrast, fewer within-host models have investigated viral replication, host–virus interactions, and the effects of immune or therapeutic mechanisms [5, 11, 16]. Epidemiological models support population-level decision-making, whereas within-host models provide complementary insight into cellular and immunological processes that determine viral persistence and disease progression.

The present study develops a within-host mathematical model describing interactions between SARS-CoV-2 and major components of the innate immune response. The model is analyzed with respect to nonnegativity, global existence, the within-host reproduction number, and the stability of the COVID-19-free equilibrium (CFE). We then calibrate unknown parameters using clinical measurements from groups with different disease severities, including mild, severe, and intensive care unit (ICU)-admitted patients. Finally, we compare simulated immune-cell and viral-load trajectories and perform a normalized sensitivity analysis of the reproduction number.

2 Innate immune response

Innate immunity constitutes the first line of defense against invading pathogens. It acts rapidly and nonspecifically to restrict pathogen entry, replication, and dissemination. The innate immune system includes macrophages, eosinophils, natural killer cells, dendritic cells, mast cells, neutrophils, basophils, and other cell populations arising from distinct developmental lineages. Many of these cells originate in the bone marrow, enter the circulation, and migrate to epithelial, mucosal, and connective tissues, where they provide immediate protection.

Granulocytes, including neutrophils, basophils, and eosinophils, contain intracellular granules that are released following activation. Neutrophils and macrophages can also engulf and destroy foreign material through phagocytosis. Enzymatic activity, phagocytosis, cytokine secretion, and cell-to-cell signaling collectively contribute to pathogen clearance and coordinate the early host response. Innate immune cells also interact closely with the adaptive immune system and influence the subsequent development of antigen-specific immunity [23].

In SARS-CoV-2 infection, innate immune mechanisms restrict viral entry, translation, replication, and assembly; promote the recognition and removal of infected cells; and support the initiation of adaptive immune responses [1]. The present model focuses on monocytes, resting and activated macrophages, and neutrophils. These populations were selected because they

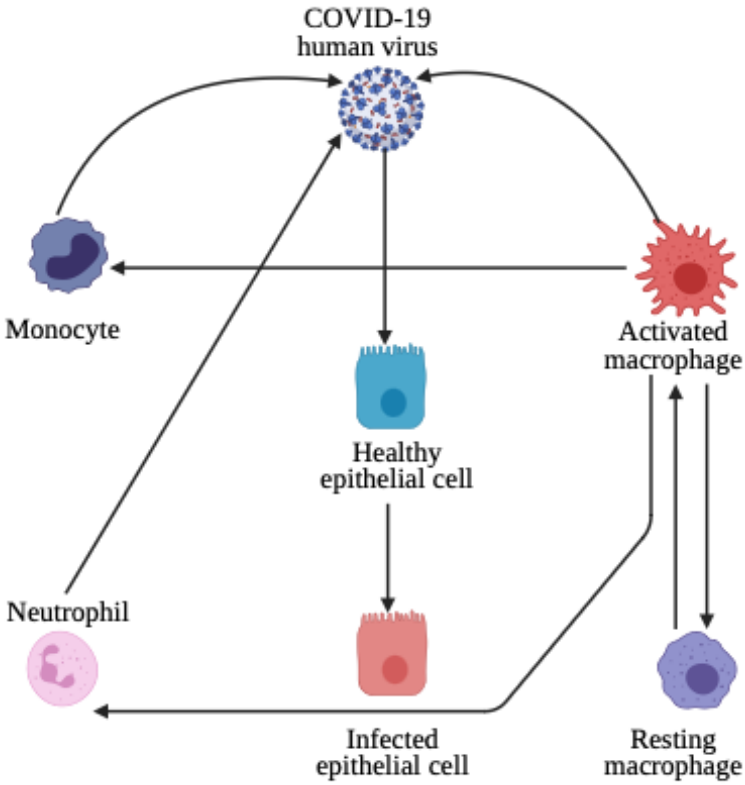

Figure 1: Key immune-cell populations involved in the innate response to SARS-CoV-2. Following exposure to the virus, resting macrophages convert into activated macrophages and can revert to the resting state through macrophage polarization [18]. Activated macrophages release signaling molecules that recruit monocytes from the circulation to the site of infection, thereby increasing macrophage numbers in affected tissues. They also secrete inflammatory mediators that enhance the activity of granulocytes such as neutrophils. The coordinated interactions among these innate immune cells help restrict viral replication and limit the spread of SARS-CoV-2.

are central to the early antiviral response and because clinical data describing neutrophil and monocyte dynamics were available for model calibration. This reduced representation yields a tractable model while retaining key features of the innate response.

3 Model construction

The proposed within-host model describes interactions among SARS-CoV-2, epithelial cells, and selected innate immune-cell populations, as illustrated in Figure 1. The state variables are $S_E(t)$, uninfected epithelial cells; $I_E(t)$, infected epithelial cells; $M_1(t)$, resting macrophages;

$M_2(t)$, activated macrophages; $C_N(t)$, neutrophils; $C_M(t)$, monocytes; and $V(t)$, free viral load. Definitions of the state variables and parameters are provided in Table 1. The within-host dynamics are described by the following nonlinear system of ordinary differential equations:

$$\begin{aligned}
\frac{dS_E}{dt} &= \psi_s - \xi S_E V - \mu_s S_E + \rho I_E,\\
\frac{dI_E}{dt} &= \xi S_E V - \mu_i I_E - \rho I_E,\\
\frac{dM_1}{dt} &= \psi_r - \alpha_r M_1 V - \mu_r M_1 + \kappa M_2,\\
\frac{dM_2}{dt} &= \alpha_r M_1 V - \mu_a M_2 - \kappa M_2 - \nu_a M_2 V,\\
\frac{dC_N}{dt} &= \psi_n M_2 C_N - \mu_n C_N - \nu_n C_N V,\\
\frac{dC_M}{dt} &= \psi_m M_2 C_M - \mu_m C_M - \nu_m C_M V,\\
\frac{dV}{dt} &= \eta \psi_v I_E - \mu_v V - \gamma_c M_2 V - \gamma_n C_N V - \gamma_m C_M V.
\end{aligned} \tag{1}$$

3.1 Biological interpretation of the proposed model

(1) **Healthy epithelial cells:** These cells form the epithelial lining of mucosal surfaces and alveolar structures. They are renewed from progenitor cells at rate ψ_s, become infected through the mass-action term $\xi S_E V$, and are lost naturally at rate $\mu_s S_E$. The term ρI_E represents recovery or replacement of infected epithelial cells before irreversible cytopathic injury.

(2) **Infected epithelial cells:** New infected cells are generated at rate $\xi S_E V$. They are removed by natural or infection-associated loss at rate $\mu_i I_E$ and return to the uninfected compartment through the recovery term ρI_E.

(3) **Resting macrophages:** Resting macrophages are recruited at rate ψ_r and are lost naturally at rate $\mu_r M_1$. Viral exposure activates them at rate $\alpha_r M_1 V$, whereas activated macrophages revert to the resting state at rate κM_2.

(4) **Activated macrophages:** Activated macrophages arise through virus-dependent activation of resting macrophages. Their population declines through natural loss and reversion at rate $(\mu_a + \kappa)M_2$, and through virus-associated loss at rate $\nu_a M_2 V$.

(5) **Neutrophils:** The term $\psi_n M_2 C_N$ represents macrophage-associated neutrophil recruitment or expansion. Neutrophils are lost naturally at rate $\mu_n C_N$ and through virus-associated loss at rate $\nu_n C_N V$.

(6) **Monocytes:** Macrophage-associated monocyte recruitment or expansion is represented by $\psi_m M_2 C_M$. Natural and virus-associated losses occur at rates $\mu_m C_M$ and $\nu_m C_M V$, respectively.

(7) **Free virus:** Viral particles are produced from infected epithelial cells at rate $\eta\psi_v I_E$. They are removed naturally at rate $\mu_v V$ and through the actions of activated macrophages, neutrophils, and monocytes at rates $\gamma_c M_2 V$, $\gamma_n C_N V$, and $\gamma_m C_M V$, respectively.

4 Basic properties of the model

4.1 Existence, positivity, and boundedness

Because the right-hand side of system (1) is locally Lipschitz continuous on $\mathbb{R}^7_+$, a unique local solution exists for every nonnegative initial condition.

Theorem 1. For every nonnegative initial condition, the solution of system (1) remains nonnegative for all times for which it exists. Moreover, the total epithelial-cell population $E = S_E + I_E$, the total macrophage population $Q = M_1 + M_2$, and the viral load V are ultimately bounded. The neutrophil and monocyte variables cannot undergo finite-time blow-up. If $\psi_n \overline{M}_2 < \mu_n$ and $\psi_m \overline{M}_2 < \mu_m$ for an eventual upper bound $\overline{M}_2$ of M_2, then C_N and C_M are also ultimately bounded.

Proof. On the boundary of the nonnegative orthant,

$$\left.\frac{dS_E}{dt}\right|_{S_E=0} = \psi_s + \rho I_E > 0, \qquad \left.\frac{dI_E}{dt}\right|_{I_E=0} = \xi S_E V \geq 0,$$
$$\left.\frac{dM_1}{dt}\right|_{M_1=0} = \psi_r + \kappa M_2 > 0, \qquad \left.\frac{dM_2}{dt}\right|_{M_2=0} = \alpha_r M_1 V \geq 0,$$
$$\left.\frac{dC_N}{dt}\right|_{C_N=0} = 0, \qquad \left.\frac{dC_M}{dt}\right|_{C_M=0} = 0,$$
$$\left.\frac{dV}{dt}\right|_{V=0} = \eta\psi_v I_E \geq 0.$$

Table 1: Definitions of the state variables and parameters used in the proposed model.

Variables	**Description**
$S_E(t)$	Population of uninfected epithelial cells
$I_E(t)$	Population of epithelial cells infected with the virus
$M_1(t)$	Population of resting macrophages
$M_2(t)$	Population of activated macrophages
$C_N(t)$	Population of neutrophils
$C_M(t)$	Population of monocytes
$V(t)$	Viral load (free virus particles)
Parameters	**Description**
ψ_v	Viral output produced from lysed infected cells
η	Rate of lysis of infected epithelial cells
γ_c	Removal of virus particles by macrophages
γ_n	Removal of virus particles by neutrophils
γ_m	Removal of virus particles by monocytes
ψ_s	Renewal of healthy epithelial cells from progenitors
ξ	Rate of viral infection of epithelial cells
μ_s	Turnover (loss) of healthy epithelial cells
μ_i	Turnover (loss) of infected epithelial cells
ψ_r	Recruitment rate of resting macrophages
α_r	Transition of resting macrophages into activated form
μ_r	Loss of resting macrophages
κ	Reversion of activated macrophages to the resting state
μ_a	Loss of activated macrophages
ν_a	Virus-driven loss of activated macrophages
ψ_n	Recruitment of neutrophils induced by macrophages
μ_n	Loss of neutrophils
ν_n	Virus-driven loss of neutrophils
ψ_m	Recruitment of monocytes induced by macrophages
μ_m	Loss of monocytes
ν_m	Virus-driven loss of monocytes
μ_v	Natural clearance rate of free virus

Thus, the vector field is inward-pointing on every boundary hyperplane, and all state variables remain nonnegative.

Let $E = S_E + I_E$ and $\mu_E = \min\{\mu_s, \mu_i\}$. Then

$$\frac{dE}{dt} = \psi_s - \mu_s S_E - \mu_i I_E \leq \psi_s - \mu_E E,$$

which implies

$$\limsup_{t\to\infty} E(t) \leq \frac{\psi_s}{\mu_E}.$$

Similarly, for $Q = M_1 + M_2$ and $\mu_Q = \min\{\mu_r, \mu_a\}$,

$$\frac{dQ}{dt} = \psi_r - \mu_r M_1 - \mu_a M_2 - \nu_a M_2 V \leq \psi_r - \mu_Q Q,$$

and therefore

$$\limsup_{t\to\infty} Q(t) \leq \frac{\psi_r}{\mu_Q}.$$

Since I_E is bounded,

$$\frac{dV}{dt} \leq \eta\psi_v I_E - \mu_v V$$

provides an ultimate bound for V. Because M_2 and V are bounded, the equations for C_N and C_M are scalar linear equations with bounded time-dependent coefficients. Hence, these variables remain finite on every finite time interval, and the local solution extends globally. The additional inequalities stated in the theorem yield exponential comparison bounds and ultimate boundedness of C_N and C_M. □

4.2 Basic reproduction number

The CFE (COVID-19-free equilibrium) is obtained by setting $I_E = M_2 = C_N = C_M = V = 0$ and solving the remaining steady-state equations:

$$E_0 = \left(\frac{\psi_s}{\mu_s}, 0, \frac{\psi_r}{\mu_r}, 0, 0, 0, 0\right).$$

For the infected variables $x = (I_E, V)^T$, the next-generation decomposition at E_0 is

$$\mathcal{F} = \begin{pmatrix} 0 & \xi\psi_s/\mu_s \\ 0 & 0 \end{pmatrix}, \qquad \mathcal{V} = \begin{pmatrix} \mu_i + \rho & 0 \\ -\eta\psi_v & \mu_v \end{pmatrix}.$$

Using the next-generation matrix method [2], the basic reproduction number is

$$R_0 = \rho(\mathcal{F}\mathcal{V}^{-1}) = \frac{\xi\psi_s\eta\psi_v}{(\mu_i + \rho)\mu_s\mu_v}. \tag{2}$$

Biologically, R_0 represents the expected number of newly infected epithelial cells generated by one infected epithelial cell in an otherwise susceptible within-host environment. It combines target-cell availability, viral entry and production, the duration of infected-cell survival, and free-virus persistence.

4.3 Local stability of the CFE

Theorem 2. The CFE E_0 is locally asymptotically stable if $R_0 < 1$ and unstable if $R_0 > 1$.

Proof. At E_0, five eigenvalues of the Jacobian are

$$-\mu_s, \qquad -\mu_r, \qquad -(\mu_a + \kappa), \qquad -\mu_n, \qquad -\mu_m.$$

The remaining two eigenvalues are those of the infected subsystem

$$A = \begin{pmatrix} -(\mu_i + \rho) & \xi\psi_s/\mu_s \\ \eta\psi_v & -\mu_v \end{pmatrix}.$$

The trace of A is negative, and

$$\det(A) = (\mu_i + \rho)\mu_v - \frac{\xi\psi_s\eta\psi_v}{\mu_s} = (\mu_i + \rho)\mu_v(1 - R_0).$$

Consequently, both eigenvalues of A have negative real parts when $R_0 < 1$. When $R_0 > 1$, $\det(A) < 0$, so A has one positive eigenvalue and E_0 is unstable. □

4.4 Global stability of the CFE

Define

$$\Omega_0 = \left\{ (S_E, I_E, M_1, M_2, C_N, C_M, V) \in \mathbb{R}^7_+ : S_E + I_E \leq \frac{\psi_s}{\mu_s} \right\}.$$

If $\mu_i \geq \mu_s$, the set Ω_0 is positively invariant for initial data satisfying $S_E(0) + I_E(0) \leq \psi_s/\mu_s$.

Theorem 3. Within Ω_0, the CFE E_0 is globally asymptotically stable whenever $R_0 \leq 1$.

Proof. Consider the Lyapunov function

$$\mathcal{L} = I_E + \frac{\mu_i + \rho}{\eta\psi_v} V.$$

Along solutions of system (1),

$$\begin{aligned} \dot{\mathcal{L}} &= \xi S_E V - (\mu_i + \rho) I_E \\ &\quad + \frac{\mu_i + \rho}{\eta\psi_v} \left(\eta\psi_v I_E - \mu_v V - \gamma_c M_2 V - \gamma_n C_N V - \gamma_m C_M V \right) \end{aligned}$$

$$\leq \left(\xi S_E - \frac{(\mu_i+\rho)\mu_v}{\eta\psi_v}\right) V.$$

Since $S_E \leq \psi_s/\mu_s$ in Ω_0,

$$\dot{\mathcal{L}} \leq \frac{(\mu_i+\rho)\mu_v}{\eta\psi_v}(R_0-1)V \leq 0$$

whenever $R_0 \leq 1$. By the boundedness results above, each trajectory in Ω_0 is contained in a compact positively invariant subset of the nonnegative state space. The largest invariant subset of $\{\dot{\mathcal{L}} = 0\}$ is characterized by $V = I_E = 0$. The remaining equations then imply

$$S_E \to \frac{\psi_s}{\mu_s}, \qquad M_1 \to \frac{\psi_r}{\mu_r}, \qquad M_2, C_N, C_M \to 0.$$

LaSalle's invariance principle therefore establishes the global asymptotic stability of E_0 in Ω_0. □

5 Simulation and discussion

Numerical simulations were performed in Julia to examine viral-load trajectories, estimate unknown parameters, and evaluate the sensitivity of R_0. Some parameter values were obtained from published studies, as summarized in Table 2, whereas parameters not available from previous within-host COVID-19 models were estimated separately for the two clinical datasets.

Table 2: Fixed parameter values used in the proposed model.

Parameter	Value	Unit	Source
$\eta\psi_v$	$1/19.03$	$\text{virus}\,\text{cell}^{-1}\,\text{day}^{-1}$	[3]
γ_c	1.31	day^{-1}	[3]
ψ_s	4×10^{-3}	$\text{cells}\,\text{mL}^{-1}\,\text{day}^{-1}$	[12]
ξ	5×10^{-9}–5.61×10^{-7}	$\text{mL}\,\text{virus}^{-1}\,\text{day}^{-1}$	[3]
μ_s	0.14	day^{-1}	[22]
μ_i	0.15	day^{-1}	[3]
ψ_r	0.02	day^{-1}	[6]
α_r	0.001	day^{-1}	[6]
μ_r	0.02	day^{-1}	[6]
κ	0.05–0.08	day^{-1}	[6]
μ_a	0.02	day^{-1}	[6]
ν_a	10^{-7}	cell^{-1}	[6]

5.1 Datasets

The first dataset, reported in [24], included 116 confirmed COVID-19 cases in Wenzhou, China, between 19 January and 20 February 2020. Twenty-seven patients were classified as severe, of whom nine required ICU treatment. Severe disease was defined using clinical criteria including elevated respiratory rate, reduced resting oxygen saturation, impaired oxygenation ($PaO_2/FiO_2 \leq 300\,\text{mmHg}$), or rapid radiographic progression. ICU admission was associated with respiratory failure requiring mechanical ventilation, circulatory shock, or multiorgan dysfunction. Neutrophil and monocyte measurements from the severe ICU and severe non-ICU subgroups were used for parameter estimation.

The second dataset, reported in [9], included 61 patients divided into mild (42 patients) and severe (19 patients) groups. Mild cases ranged from limited symptoms without radiographic pneumonia to fever and respiratory symptoms with imaging-confirmed pneumonia. Severe cases met criteria similar to those used in the first dataset. In the remainder of this study, the first and second datasets are denoted by ref1 and ref2, respectively.

5.2 Parameter estimation

Table 3: Estimated parameter values for the different clinical groups.

Parameter	**Severe ICU (ref1)**	**Severe (ref1)**	**Mild (ref2)**	**Severe (ref2)**	**Unit**	**Source**
γ_n	0.05	0.05	0.1	0.05	day^{-1}	Estimated
γ_m	0.05	0.093	0.1	0.05	day^{-1}	Estimated
ρ	0.05	0.0025	0.05	4.1×10^{-10}	day^{-1}	Estimated
ψ_n	0.17	0.338	0.0096	0.08	model-specific	Estimated
μ_n	0.093	0.196	0.0156	0.076	day^{-1}	Estimated
ν_n	8.5	5.7×10^{-8}	0.5	8.5	model-specific	Estimated
ψ_m	0.15	0.294	0.096	0.053	model-specific	Estimated
μ_m	0.08	0.164	0.0359	0.028	day^{-1}	Estimated
ν_m	0.5	0.5	0.01	0.1	model-specific	Estimated
μ_v	0.03	0.03	0.29	0.03	day^{-1}	Estimated

Unknown parameters were estimated independently for each severity group. For each dataset, the objective function was defined as the sum of squared differences between the observed neutrophil and monocyte measurements and the corresponding model outputs. A genetic algorithm was used to explore the nonlinear parameter space because the objective function may be multimodal and the parameters may interact strongly.

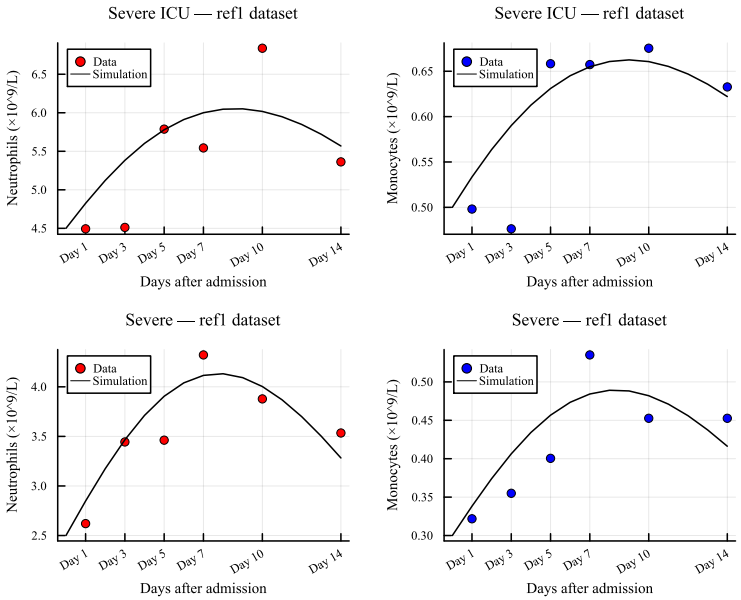

(a)

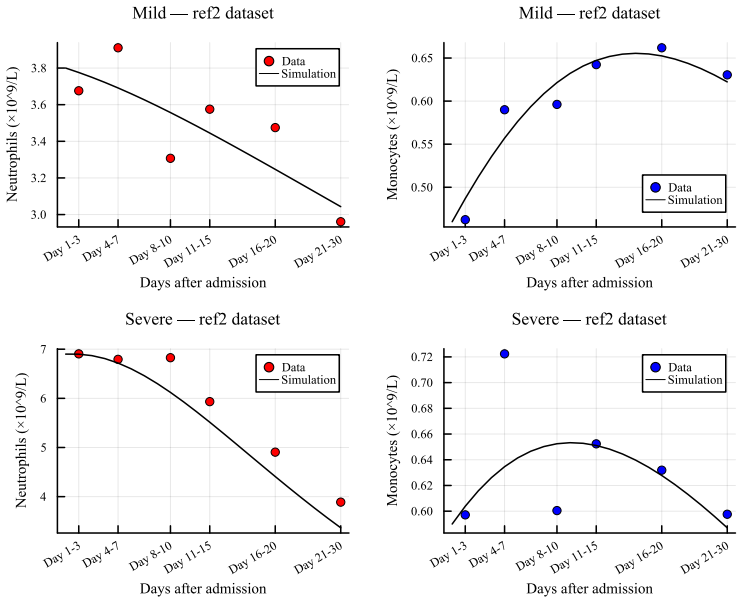

(b)

Figure 2: Goodness of fit between model simulations and clinical data. (a) Results based on dataset ref1, showing monocyte and neutrophil dynamics in severe and severe ICU patients. (b) Results based on dataset ref2, showing monocyte and neutrophil dynamics in mild and severe patients. In both datasets, the model reproduces the observed temporal patterns, indicating good agreement with the clinical data.

Table 3 summarizes the estimated values, and Figure 2 compares the model simulations with the clinical observations. Because only a limited number of group-level time points were available, the fitted curves should be interpreted as calibrated representations of the reported temporal patterns rather than as individual-patient predictions.

5.3 Estimated parameters and disease severity

Figure 3 highlights differences in the estimated parameters after normalization relative to the mild group. Neutrophil-mediated viral clearance (γ_n) was greatest in the mild ref2 group. Monocyte-mediated viral clearance (γ_m) was also high in the mild ref2 and severe ref1 groups, suggesting that effective monocyte activity may contribute to viral control in some noncritical cases. The epithelial recovery parameter ρ was substantially lower in severe ref1 and nearly zero in severe ref2 patients, indicating impaired epithelial restoration in these groups.

Neutrophil recruitment or expansion (ψ_n) and natural loss (μ_n) were highest in severe ref1 patients, consistent with a highly dynamic and potentially dysregulated neutrophil response. Virus-associated neutrophil loss (ν_n) varied markedly across groups and was high in severe ICU ref1 and severe ref2 patients but negligible in severe ref1. This large between-dataset variability may reflect cohort differences, limited sampling, or practical parameter-identifiability constraints. Monocyte recruitment or expansion (ψ_m) was greater in severe ref1 than in severe ICU ref1 and was higher in mild than severe ref2. Virus-associated monocyte loss (ν_m) was substantially lower in the mild group than in either ref1 severe group. Finally, the natural viral-clearance rate μ_v was much higher in mild ref2 than in the other groups.

Overall, the estimated parameter patterns support a cautious interpretation: mild disease is associated with more efficient viral clearance and epithelial recovery, whereas severe disease is characterized by impaired repair and dysregulated immune-cell turnover. Recruitment estimates do not change monotonically with severity; therefore, elevated recruitment should not automatically be interpreted as an effective response, because excessive innate-cell activation may coexist with tissue injury.

5.4 Initial conditions

The initial-condition vector was ordered as

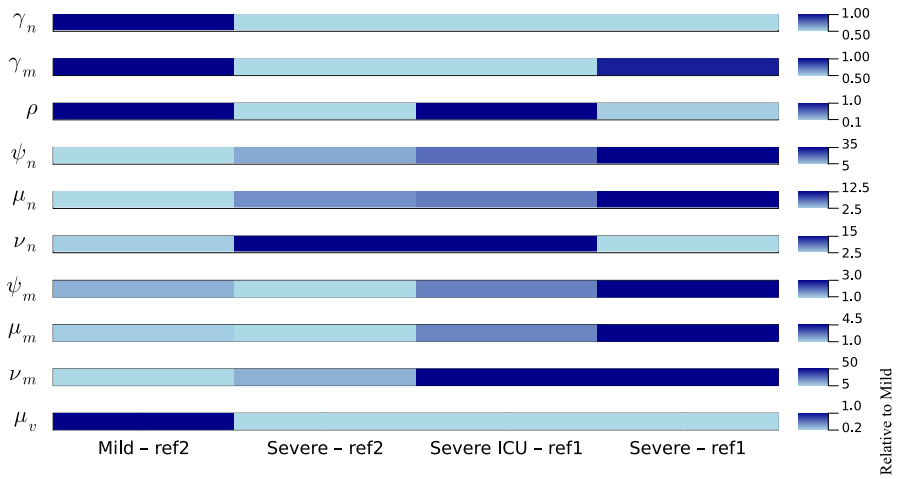

Figure 3: Estimated parameter patterns across the clinical groups. Mild cases show stronger natural viral clearance (μ_v) and more effective epithelial recovery (ρ). Severe and ICU cases show impaired epithelial repair, heterogeneous neutrophil and monocyte recruitment or expansion (ψ_n, ψ_m), and, in several groups, increased virus-associated immune-cell loss (ν_n, ν_m). The recruitment parameters do not vary monotonically with disease severity.

$$u_0 = [S_E(0), I_E(0), M_1(0), M_2(0), C_N(0), C_M(0), V(0)].$$

The values were selected using the reported severity-dependent immune-cell measurements and values adopted in related within-host models [7, 10, 25]. For both severe ICU and severe non-ICU groups in ref1, we used

$$u_0 = [0.4, 3 \times 10^{-8}, 0, 1, 2.5, 0.3, 357 \times 10^{-6}].$$

For the mild ref2 group, we used

$$u_0 = [0.4, 3 \times 10^{-8}, 0, 1, 3.8, 0.46, 357 \times 10^{-6}],$$

whereas the severe ref2 group was initialized with

$$u_0 = [0.4, 3 \times 10^{-8}, 0, 1, 6.9, 0.59, 357 \times 10^{-6}].$$

These initial conditions reproduce the baseline differences reported for the patient groups and should be interpreted as group-level calibration inputs rather than individualized clinical states.

5.5 Dynamics of neutrophils, monocytes, and viral load across severity groups

Figure 4 compares the simulated neutrophil, monocyte, and viral-load trajectories for the four severity groups. Viral load is displayed on a $\log_{10}$ scale. All groups exhibit an early decline, but the mild ref2 group maintains the lowest viral burden and shows the fastest overall clearance. The severe groups display slower clearance and retain higher viral loads over much of the simulated period. Because treatment information was not explicitly included in the model, differences in the simulated decline should be interpreted as consequences of the calibrated parameter sets rather than as direct effects of intensive-care management or specific therapies.

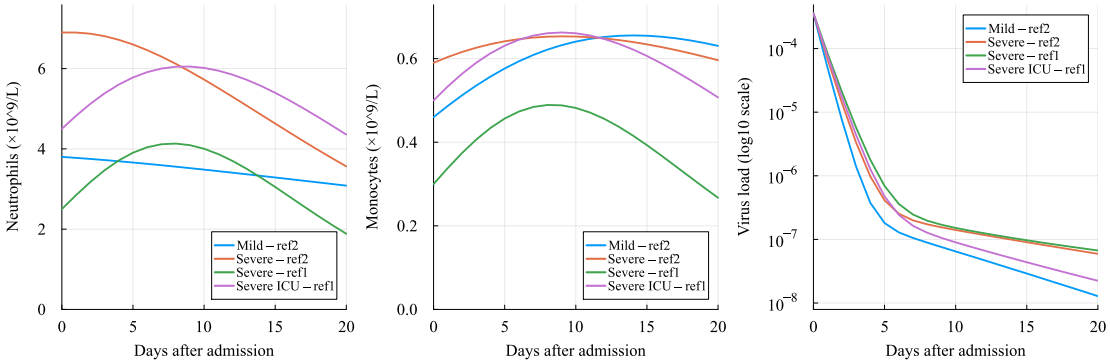

Figure 4: Simulated trajectories of neutrophils (left), monocytes (middle), and viral load (right) for patient groups of varying severity from datasets ref1 and ref2. Mild cases (ref2) show lower and more stable neutrophil counts, sustained monocyte levels, and the fastest viral clearance. Severe and ICU cases exhibit elevated neutrophils, altered monocyte dynamics, and delayed viral clearance, with severe ref1 patients retaining the highest viral load throughout the simulation.

The immune-cell trajectories also differ among groups. Neutrophil levels are lowest and comparatively stable in mild ref2 patients. Severe ref1 patients show a pronounced increase followed by a decline, whereas severe ICU ref1 and severe ref2 patients maintain elevated neutrophil levels. These patterns are consistent with a dysregulated neutrophil response in severe disease, although the simulations alone cannot establish a causal relationship with tissue injury.

Monocyte levels remain comparatively sustained in mild ref2, severe ref2, and severe ICU ref1 groups, whereas severe ref1 patients show lower overall levels. Taken together, the model-calibrated trajectories associate mild disease with rapid viral clearance and more controlled immune-cell dynamics, while severe and ICU disease is associated with delayed clearance and heterogeneous innate immune responses.

5.6 Sensitivity analysis

The normalized forward sensitivity index of R_0 with respect to a parameter ω is defined by

$$\Upsilon_{\omega}^{R_0} = \frac{\partial R_0}{\partial \omega}\frac{\omega}{R_0}.$$

A positive index indicates that an increase in the parameter increases R_0, whereas a negative index indicates that an increase decreases R_0. From equation (2), the indices are

$$\Upsilon_{\xi}^{R_0} = 1, \quad \Upsilon_{\psi_s}^{R_0} = 1, \quad \Upsilon_{\eta}^{R_0} = 1, \quad \Upsilon_{\psi_v}^{R_0} = 1,$$
$$\Upsilon_{\mu_s}^{R_0} = -1, \quad \Upsilon_{\mu_v}^{R_0} = -1, \quad \Upsilon_{\mu_i}^{R_0} = -\frac{\mu_i}{\mu_i+\rho}, \quad \Upsilon_{\rho}^{R_0} = -\frac{\rho}{\mu_i+\rho}.$$

Thus, viral entry (ξ), healthy epithelial-cell renewal (ψ_s), infected-cell lysis (η), and viral output (ψ_v) increase R_0 proportionally. In contrast, greater healthy-cell loss (μ_s), free-virus clearance (μ_v), infected-cell loss (μ_i), and epithelial recovery (ρ) reduce R_0. The indices of ξ, ψ_s, η, ψ_v, μ_s, and μ_v are exactly ± 1 and therefore do not vary among the severity groups. Only the relative negative contributions of μ_i and ρ vary because ρ is group-specific.

For severe ICU ref1 and mild ref2, $\rho = 0.05$ gives

$$\Upsilon_{\mu_i}^{R_0} = -0.75, \qquad \Upsilon_{\rho}^{R_0} = -0.25.$$

For severe ref1, the corresponding indices are approximately -0.984 and -0.016, respectively. For severe ref2, the near-zero value of ρ makes $\Upsilon_{\mu_i}^{R_0}$ approximately -1 and $\Upsilon_{\rho}^{R_0}$ approximately zero. Figure 5 displays these corrected indices.

The sensitivity analysis was performed using the normalized-index approach applied in [15]. The results identify viral entry and production as direct promoters of within-host infection. Conversely, reducing viral entry or production, accelerating free-virus clearance, or improving the recovery and removal of infected epithelial cells is predicted to reduce R_0.

6 Conclusion

We developed and analyzed a within-host mathematical model describing interactions among SARS-CoV-2, epithelial cells, macrophages, neutrophils, and monocytes. The model preserves nonnegativity and admits a biologically meaningful CFE. The within-host basic reproduction number is determined by target-cell availability, viral entry and production, infected-cell recovery or loss, and free-virus clearance. Local stability analysis shows that the CFE is stable when

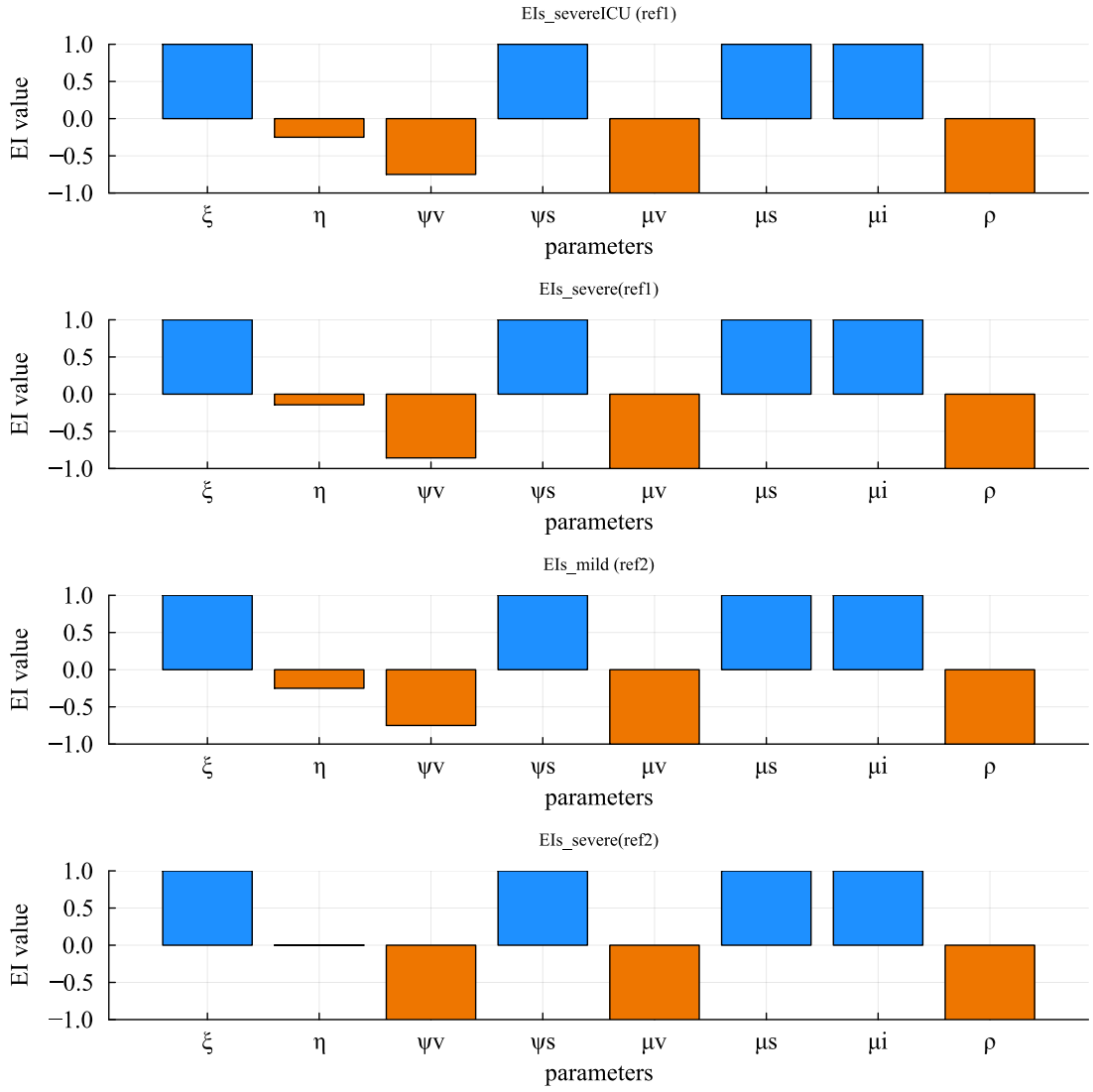

Figure 5: Normalized sensitivity indices of R_0 with respect to the model parameters, represented using a tornado diagram. Positive indices identify parameters that increase within-host viral reproduction, whereas negative indices identify parameters that reduce it.

$R_0 < 1$, and a Lyapunov argument establishes global stability in the stated invariant region when $R_0 \leq 1$.

Calibration to two clinical datasets revealed severity-dependent patterns. Mild disease was associated with faster viral clearance, greater epithelial recovery, and more controlled neutrophil

behavior. Severe and ICU groups exhibited delayed clearance, heterogeneous recruitment, and greater virus-associated immune-cell loss. The corrected normalized sensitivity analysis shows that viral entry and production increase R_0, whereas viral clearance, infected-cell recovery, and cell-loss mechanisms decrease it.

These results demonstrate how within-host mathematical modeling can integrate clinical immune-cell measurements and generate mechanistic hypotheses regarding COVID-19 severity. Extension of the model to adaptive immunity, treatment, host heterogeneity, and patient-level uncertainty may provide broader insight into SARS-CoV-2 and related respiratory viral infections.

Funding

This research received no external funding.

Conflicts of Interest

The authors declare no conflicts of interest.

References

[1] Diamond, M.S. and Kanneganti, T.D., *Innate immunity: The first line of defense against SARS-CoV-2*, Nat. Immunol., 23(2) (2022), 165–176. 10.1038/s41590-021-01091-0.

[2] Diekmann, O., Heesterbeek, J.A.P. and Metz, J.A.J., *On the definition and the computation of the basic reproduction ratio R_0 in models for infectious diseases in heterogeneous populations*, J. Math. Biol., 28(4) (1990), 365–382. 10.1007/BF00178324.

[3] Dogra, P., Ruiz-Ramírez, J., Sinha, K., Butner, J.D., Peláez, M.J., Rawat, M., Yellepeddi, V.K., Pasqualini, R., Arap, W., Sostman, H.D. and Cristini, V., *Innate immunity plays a key role in controlling viral load in COVID-19: Mechanistic insights from a whole-body infection dynamics model*, ACS Pharmacol. Transl. Sci., 4(1) (2021), 248–265. 10.1021/acsptsci.0c00183.

[4] Dos Santos, W.G., *Impact of virus genetic variability and host immunity for the success of COVID-19 vaccines*, Biomed. Pharmacother., 136 (2021), 111272. 10.1016/j.biopha.2021.111272.

[5] Du, S.Q. and Yuan, W., *Mathematical modeling of interaction between innate and adaptive immune responses in COVID-19 and implications for viral pathogenesis*, J. Med. Virol., 92(9) (2020), 1615–1628. 10.1002/jmv.25866.

[6] Eftimie, R. and Hamam, H., *Modelling and investigation of the $CD4^+$ T cells–macrophages paradox in melanoma immunotherapies*, J. Theor. Biol., 420 (2017), 82–104. 10.1016/j.jtbi.2017.02.022.

[7] Ghosh, I., *Within-host dynamics of SARS-CoV-2 in humans: Modeling immune responses and antiviral treatments*, SN Comput. Sci., 2(6) (2021), 482. 10.1007/s42979-021-00919-8.

[8] Giordano, G., Blanchini, F., Bruno, R., Colaneri, P., Di Filippo, A., Di Matteo, A. and Colaneri, M., *Modelling the COVID-19 epidemic and implementation of population-wide interventions in Italy*, Nat. Med., 26(6) (2020), 855–860. 10.1038/s41591-020-0883-7.

[9] Guan, J., Wei, X., Qin, S., Liu, X., Jiang, Y., Chen, Y., Chen, Y., Lu, H., Qian, J., Wang, Z. and Lin, X., *Continuous tracking of COVID-19 patients' immune status*, Int. Immunopharmacol., 89(Pt A) (2020), 107034. 10.1016/j.intimp.2020.107034.

[10] Han, M., Xu, M., Zhang, Y., Liu, Z., Li, S., He, T., Li, J., Gao, Y., Liu, W., Li, T. and Chen, Z., *Assessing SARS-CoV-2 RNA levels and lymphocyte/T-cell counts in COVID-19 patients revealed initial immune status as a major determinant of disease severity*, Med. Microbiol. Immunol., 209 (2020), 657–668. 10.1007/s00430-020-00693-z.

[11] Hernandez-Vargas, E.A. and Velasco-Hernandez, J.X., *In-host mathematical modelling of COVID-19 in humans*, Annu. Rev. Control, 50 (2020), 448–456. 10.1016/j.arcontrol.2020.09.006.

[12] Hernandez-Vargas, E.A. and Velasco-Hernandez, J.X., *In-host modelling of COVID-19 kinetics in humans*, medRxiv preprint (2020). 10.1101/2020.03.26.20044487.

[13] Mack, A., Choffnes, E.R., Hamburg, M.A. and Relman, D.A., editors, *Microbial Evolution and Co-Adaptation: A Tribute to the Life and Scientific Legacies of Joshua Lederberg: Workshop Summary*, National Academies Press, Washington, DC, 2009. 10.17226/12586.

[14] Ivorra, B., Ferrández, M.R., Vela-Pérez, M. and Ramos, A.M., *Mathematical modeling of the spread of coronavirus disease 2019 (COVID-19) taking into account undetected infections: The case of China*, Commun. Nonlinear Sci. Numer. Simul., 88 (2020), 105303. 10.1016/j.cnsns.2020.105303.

[15] Jabbari, A., Lotfi, M., Kheiri, H. and Khajanchi, S., *Mathematical analysis of the dynamics of a fractional-order tuberculosis epidemic in a patchy environment under the influence of re-infection*, Math. Methods Appl. Sci., 46(17) (2023), 17798–17817. 10.1002/mma.9532.

[16] Li, C., Xu, J., Liu, J. and Zhou, Y., *The within-host viral kinetics of SARS-CoV-2*, Math. Biosci. Eng., 17(4) (2020), 2853–2861. 10.3934/mbe.2020159.

[17] McNeill, W.H., *Plagues and Peoples*, Anchor Press, Garden City, NY, 1976.

[18] Murray, P.J., Allen, J.E., Biswas, S.K., Fisher, E.A., Gilroy, D.W., Goerdt, S., Gordon, S., Hamilton, J.A., Ivashkiv, L.B., Lawrence, T. and Locati, M., *Macrophage activation and polarization: Nomenclature and experimental guidelines*, Immunity, 41(1) (2014), 14–20. 10.1016/j.immuni.2014.06.008.

[19] Musa, S.S., Qureshi, S., Zhao, S., Yusuf, A., Mustapha, U.T. and He, D., *Mathematical modeling of COVID-19 epidemic with effect of awareness programs*, Infect. Dis. Model., 6 (2021), 448–460. 10.1016/j.idm.2021.01.012.

[20] Ndaïrou, F., Area, I., Nieto, J.J. and Torres, D.F.M., *Mathematical modeling of COVID-19 transmission dynamics with a case study of Wuhan*, Chaos Solitons Fractals, 135 (2020), 109846. 10.1016/j.chaos.2020.109846.

[21] Peng, L., Yang, W., Zhang, D., Zhuge, C. and Hong, L., *Epidemic analysis of COVID-19 in China by dynamical modeling*, arXiv preprint arXiv:2002.06563 (2020).

[22] Sasmal, S.K., Dong, Y. and Takeuchi, Y., *Mathematical modeling on T-cell-mediated adaptive immunity in primary dengue infections*, J. Theor. Biol., 429 (2017), 229–240. 10.1016/j.jtbi.2017.06.035.

[23] Schultze, J.L. and Aschenbrenner, A.C., *COVID-19 and the human innate immune system*, Cell, 184(7) (2021), 1671–1692. 10.1016/j.cell.2021.02.029.

[24] Sun, S., Cai, X., Wang, H., He, G., Lin, Y., Lu, B., Chen, C., Pan, Y. and Hu, X., *Abnormalities of the peripheral blood system in patients with COVID-19 in Wenzhou, China*, Clin. Chim. Acta, 507 (2020), 174–180. 10.1016/j.cca.2020.04.024.

[25] Tavares, J.N. and Gomes, E., *COVID-19 immunotherapy: A mathematical model*, Math. Med. Biol., 40(2) (2023), 199–221. 10.1093/imammb/dqad003.

[26] World Health Organization, *Weekly epidemiological update on COVID-19: 13 July 2021*, World Health Organization, Geneva, 2021. Available from: https://www.who.int/publications/m/item/weekly-epidemiological-update-on-covid-19---13-july-2021.